Inorganic Chemistry

Photophysical Behavior of Open-Shell First-Row Transition-Metal Octabutoxynaphthalocyanines: CoNc(OBu)$_8$ and CuNc(OBu)$_8$ as Case Studies

Alexandra V. Soldatova,[†,||] **Junhwan Kim,**[‡] **Angela Rosa,**[*,§] **Giampaolo Ricciardi,**[*,§] **Malcolm E. Kenney,**[*,‡] **and Michael A. J. Rodgers**[*,†]

Center for Photochemical Sciences and Department of Chemistry, Bowling Green State University, Bowling Green, Ohio 43403, Department of Chemistry, Case Western Reserve University, Cleveland, Ohio 44106, and Dipartimento di Chimica, Università della Basilicata, Via N. Sauro 85, 85100 Potenza, Italy

Ultrafast photodynamics and density functional theory/time-dependent density functional theory (DFT/TDDFT) results for complexes of Co and Cu with 5,9,14,18,23,27,32,36-octabutoxynaphthalocyanine [CoNc(OBu)$_8$ and CuNc(OBu)$_8$] are reported. As a basis for this work, details concerning the syntheses of these complexes and the corresponding Zn complex (used as a reference) are given. Transient absorption spectrometry with femtosecond time resolution combined with a detailed DFT/TDDFT analysis has been employed to construct a complete picture of the excited-state dynamics after Q-band excitation of the Co and Cu complexes and to gain an understanding of the relationship between the nature of the metal center and the excited-state lifetime. The Co complex was shown to return to its ground state via two competing channels: a $^2T_1(\pi, \pi^*)$ state that decayed with a lifetime of 1 ps and a low-lying $^2(d, d)$ state that repopulated the ground-state surface with a lifetime of 15 ps. CuNc(OBu)$_8$ showed ground-state repopulation from the $^2T_1(\pi, \pi^*)$ state via a lower-lying ligand-to-metal charge-transfer (LMCT) state that was completed within a few nanoseconds. The photophysical behavior of the cobalt and copper complexes was compared to that previously reported for the nickel analog in an effort to highlight the effect of the central metal on the nature and rates of the deactivation pathways. The results described in this work provide basic knowledge that is relevant to the use of these compounds as photothermal sensitizers in cancer therapy.

Introduction

Since their discovery in the early 20th century, metallophthalocyanines (MPc's) have found diverse applications[1] as a result of the inherent chemical flexibility of the metallomacrocycle, which allows modulation of their physicochemical properties through ligand and metal modification. One particular application of phthalocyanines to date lies in the field of photomedicine as it relates to cancer treatment. In photodynamic therapy, for example, MPc's have been shown to have great potential, and some of them are already in phase-I clinical trials.[2–6] Recent results on one potential phototherapeutic compound from the Pc family, Ni(II) octabutoxynaphthalocyanine [NiNc(OBu)$_8$], indicate that after this compound is taken up by cancer cells, it can cause destruction of these cells through photothermal events.[7–9]

* To whom correspondence should be addressed. E-mail: rosa@unibas.it (A.R.), rg010sci@unibas.it (G.R.), malcolm.kenney@case.edu (M.E.K.), rodgers@bgnet.bgsu.edu (M.A.J.R.).

† Bowling Green State University.

‡ Case Western Reserve University.

§ Università della Basilicata.

|| Present address: Department of Chemistry, University of Washington, Seattle, WA 98195.

(1) *Phthalocyanines: Properties and Applications*; Leznoff, C. C., Lever, A. B. P., Eds.; VCH Publishers: New York, 1990–1996; Vols. *1–4*.

(2) Szacilowski, K.; Macyk, W.; Drzawiecka-Matuszek, A.; Brindell, M.; Stochel, G. *Chem. Rev.* **2005**, *105*, 2647.

(3) Ali, H.; Lier, J. E. *Chem. Rev.* **1999**, *99*, 2379.

(4) Lukyanets, E. A. *J. Porphyrins Phthalocyanines* **1999**, *3*, 424.

(5) Rosenthal, I. *J. Photochem. Photobiol.* **1991**, *53*, 859.

(6) Nyman, E. S.; Hynninen, P. H. *J. Photochem. Photobiol., B* **2004**, *73*, 1.

(7) Busetti, A.; Soncin, M.; Reddi, E.; Rodgers, M. A. J.; Kenney, M. E.; Jori, G. *J. Photochem. Photobiol. B* **1999**, *53*, 103.

(8) Camerin, M.; Rello, S.; Villanueva, A.; Ping, X.; Kenney, M. E.; Rodgers, M. A. J.; Jori, G. *Eur. J. Cancer* **2005**, *41*, 1203.

(9) Camerin, M.; Rodgers, M. A. J.; Kenney, M. E.; Jori, G. *Photochem. Photobiol. Sci.* **2005**, *4*, 251.

It is generally understood that for a compound to be an effective photothermal agent, it not only should possess high photostability and strong absorption in the phototherapeutic spectral window but also should be able to very rapidly return to its ground state after photoexcitation, thus generating a vibrationally hot ground-state molecule. $NiNc(OBu)_8$ is a typical example of a molecule that undergoes ultrafast radiationless deactivation of its excited states after photon absorption. We recently investigated the excited-state deactivation mechanism of $NiNc(OBu)_8$ using ultrafast measurements and density functional theory/time-dependent density functional theory (DFT/TDDFT) calculations.[10] Transient absorption results showed that after photoexcitation of $NiNc(OBu)_8$ in toluene, ground-state repopulation occurred with a lifetime of 500 ps. Integration of the TDDFT and experimental results indicated that the photoproduced $S_1(\pi, \pi^*)$ excited state undergoes fast deactivation through a cascade of events involving the lower-lying $^3(d_{z^2}, d_{x^2-y^2})$, $T_1(\pi, \pi^*)$, and $^3LMCT(\pi, d_{x^2-y^2})$ excited states. The close proximity of the $^3(d_{z^2}, d_{x^2-y^2})$ and $S_1(\pi, \pi^*)$ states facilitates the process of intersystem crossing to the triplet manifold, with the first observed transient being a vibrationally excited $T_1(\pi, \pi^*)$ state. After vibrational relaxation, the $T_1(\pi, \pi^*)$ state converts rapidly and reversibly into the $^3LMCT(\pi, d_{x^2-y^2})$ state. The equilibrium state so generated decays to the ground state with a lifetime of ~500 ps.

The deactivation mechanism proposed for $NiNc(OBu)_8$ indicated that the relative positions of the metal-centered (MC) and ligand-to-metal charge-transfer (LMCT) excited states with respect to either the photogenerated $S_1(\pi, \pi^*)$ state or the $T_1(\pi, \pi^*)$ state are crucial for fast dissipation of the photon energy by thermal radiationless events. The number and energies of MC, LMCT, and MLCT excited states lying below the $S_1(\pi, \pi^*)$ state depend on the central metal. Therefore, the photodeactivation mechanism and hence the efficiency of $MNc(OBu)_8$ complexes as photothermal sensitizers is expected to vary upon replacement of nickel by other first-row transition metals. In the present work, the deactivation mechanisms of the photoexcited cobalt(II) and copper(II) octabutoxynaphthalocyanine derivatives, $CoNc(OBu)_8$ and $CuNc(OBu)_8$, both of which have a doublet ground state, are reported for the first time and compared with the mechanism recently reported for the Ni(II) complex.

The excited-state spectral and dynamic behaviors of the title complexes have been investigated by ultrafast transient absorption spectroscopy and interpreted with the aid of TDDFT calculations of the doublet and quartet excited states lying below the photogenerated $^2S_1(\pi, \pi^*)$ state. The properties of the quartet excited states, which involve spin-flip (SF) transitions, have been studied using a TDDFT formalism based on the noncollinear representation of the

Scheme 1. Synthetic Route for Metal Naphthalocyanines
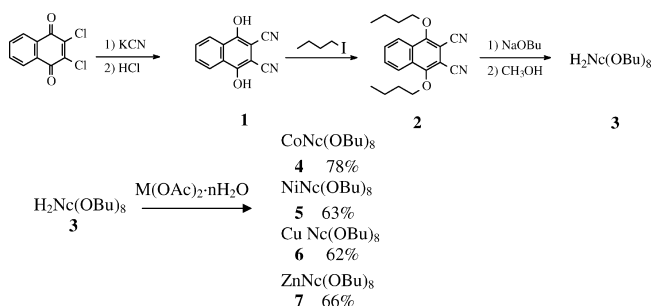
exchange-correlation (XC) potential[11,12] and recently implemented in the Amsterdam Density Functional (ADF) code.[13]

Experimental Section

A. Materials for Photochemical Studies. The solvents toluene (99.5+%, Aldrich spectrophotometric grade), benzene (99%, Aldrich HPLC grade), dichloromethane (99%, Aldrich HPLC grade), and benzonitrile (99%, Aldrich HPLC grade) were used as received.

B. Synthesis of Naphthalocyanines. Metal naphthalocyanines were prepared by metal insertion reactions, as shown in Scheme 1. Full descriptions of the syntheses are given in ref 14.

1,4-Dihydroxy-2,3-naphthalenedicarbonitrile (1).[15] **1** is a yellow-white solid that is soluble in dimethylformamide, slightly soluble in CH_2Cl_2, and insoluble in toluene and hexanes. Yield: 4.1 g, 85%. NMR [50:1 $CDCl_3-(CD_3)_2SO$]: δ 8.07 (m, 2H, 5,8-ArH), 7.44 (m, 2H, 6,7-ArH).

1,4-Dibutoxy-2,3-naphthalenedicarbonitrile (2).[16,17] **2** is a white solid that is soluble in CH_2Cl_2, dimethylformamide, toluene, and hexanes. Yield: 5.0 g, 80%. NMR ($CDCl_3$): δ 8.25 (m, 2H, 5,8-ArH), 7.78 (m, 2H, 6,7-ArH), 4.45 (t, 4H, OCH_2), 1.95 (m, 4H, OCH_2CH_2), 1.62 (m, 4H, $OC_2H_4CH_2$), 1.04 (t, 6H, $OC_3H_6CH_3$).

$H_2Nc(OBu)_8$ (3).[16,17] Under Ar, a mixture of nitrile **2** (4.7 g) and a solution of $NaOCH_3$ in CH_3OH (0.50 M, 18 mL), which had been diluted with 1-butanol (30 mL) and then distilled until free of CH_3OH, was slowly distilled (5 h, 25 mL of distillate), diluted with CH_3OH (30 mL), and filtered. The brown solid was washed in CH_3OH, chromatographed using Al_2O_3-III and toluene, vacuum-dried at room temperature, and weighed. **3** is soluble in CH_2Cl_2, dimethylformamide, and toluene and slightly soluble in hexanes. Yield: 3.1 g, 65%. UV–vis (toluene): λ_{max} (log ϵ) 864 nm (5.5). NMR ($CDCl_3$): δ 8.94 (m, 8H, 1,4-NcH), 7.86 (m, 8H, 2,3-NcH), 5.13 (t, 16H, OCH_2), 2.21 (m, 16H, OCH_2CH_2), 1.64 (m, 16H, $OC_2H_4CH_2$), 1.01 (t, 24H, $OC_3H_6CH_3$). HRMS−ESI−TOF for $[M]^+$ with M as $C_{80}H_{90}N_8O_8$: calcd, m/z 1290.6881; found, m/z 1290.6825.

$CoNc(OBu)_8$ (4).[18] Under Ar, a mixture of naphthalocyanine **3** (42 mg), $Co(CH_3CO_2)_2 \cdot 4H_2O$ (12 mg), 1,8-diazabicyclo[5.4.0]undec-7-ene (0.02 mL), and 1-butanol (2 mL) was refluxed for 2 h, diluted with a solution of CH_3OH and H_2O (1:1, 6 mL), and filtered. The green solid was chromatographed using Al_2O_3-III and toluene, rechromatographed using Al_2O_3-III and 10:1 hexanes−tetrahydrofuran,

(10) Soldatova, A. V.; Kim, K.; Peng, X.; Rosa, A.; Ricciardi, G.; Kenney, M. E.; Rodgers, M. A. J. *Inorg. Chem.* **2007**, *46*, 2080.

(11) Wang, F.; Ziegler, T. *J. Chem. Phys.* **2004**, *121*, 12191.

(12) Wang, F.; Ziegler, T. *J. Chem. Phys.* **2005**, *122*, 074109.

(13) *ADF2006.01*; Scientific Computing & Modelling NV: Amsterdam, 2006; available from http://www.scm.com.

(14) Kim, J. Ph.D. Thesis, Case Western Reserve University, 2006.

(15) Reynolds, G. A.; Vanallan, J. A. *J. Org. Chem.* **1964**, *29*, 3591.

(16) Rihter, B. D.; Kenney, M. E.; Ford, W. E.; Rodgers, M. A. J. *J. Am. Chem. Soc.* **1993**, *115*, 8146.

(17) Cook, M. J.; Dunn, A. J.; Howe, S. D.; Thomson, A. J.; Harrison, K. J. *J. Chem. Soc., Perkin Trans.* **1988**, *1*, 2453.

(18) Gao, D.; Zhao, H.; Huo, L.; Zhao, J. G.; Wu, Y. Q.; Xi, S. Q. *Sens. Actuators, B* **2004**, *97*, 319.

vacuum-dried at room temperature, and weighed. **4** is soluble in CH_2Cl_2, dimethylformamide, and toluene and slightly soluble in hexanes. Yield: 35 mg, 78%. UV–vis (toluene): λ_{max} (log ϵ) 830 nm (4.6). HRMS−ESI−TOF for [M]$^+$ with M as $C_{80}H_{88}N_8O_8{}^{59}Co$: calcd, *m/z* 1347.6057; found, *m/z* 1347.6029.

NiNc(OBu)$_8$ (5). See ref 10.

CuNc(OBu)$_8$ (6).[19] Under Ar, a mixture of naphthalocyanine **3** (110 mg), $Cu(CH_3CO_2)_2 \cdot H_2O$ (23 mg), 1,8-diazabicyclo[5.4.0]undec-7-ene (0.05 mL), and 1-butanol (5 mL) was refluxed for 20 h, diluted with a solution of CH_3OH and H_2O (1:1, 15 mL), and filtered. The brown solid was chromatographed using Al_2O_3-V and toluene, vacuum-dried at room temperature, and weighed. **6** is soluble in CH_2Cl_2, dimethylformamide, and toluene and slightly soluble in hexanes. Yield: 72 mg, 62%. UV–vis (toluene): λ_{max} (log ϵ) 850 nm (5.4). HRMS−ESI−TOF for [M]$^+$ with M as $C_{80}H_{88}N_8O_8{}^{63}Cu$: calcd, *m/z* 1351.6022; found, *m/z* 1351.5986.

ZnNc(OBu)$_8$ (7).[20] Under Ar, a mixture of naphthalocyanine **3** (100 mg), $Zn(CH_3CO_2)_2 \cdot 2H_2O$ (23 mg), 1,8-diazabicyclo[5.4.0]undec-7-ene (0.05 mL), and 1-butanol (5 mL) was refluxed for 4 h, diluted with a solution of CH_3OH and H_2O (1:1, 15 mL), and filtered. The brown solid was chromatographed using Al_2O_3-III and 1:1 tetrahydrofuran−hexanes, rechromatographed using Al_2O_3-III and 1:5 tetrahydrofuran−hexanes, vacuum-dried at room temperature, and weighed. **7** is soluble in CH_2Cl_2, dimethylformamide, and toluene and slightly soluble in hexanes. Yield: 69 mg, 66%. UV–vis (toluene): λ_{max} (log ϵ) 846 nm (4.9). NMR (CDCl$_3$): δ 9.00 (m, 8H, 1,4-NcH), 7.88 (m, 8H, 2,3-NcH), 5.25 (t, 16H, OCH$_2$), 2.25 (m, 16H, OCH$_2$CH_2), 1.68 (m, 16H, OC$_2$H$_4$CH_2), 1.05 (t, 24H, OC$_3$H$_6$CH_3). HRMS−ESI−TOF for [M]$^+$ with M as $C_{80}H_{88}$-$N_8O_8{}^{64}Zn$: calcd, *m/z* 1352.6017; found, *m/z* 1352.6024.

C. UV–Visible and Near-IR Absorption Spectra. Ground-state electronic absorption spectra in the visible region were recorded using a Varian Cary 50 Bio UV–vis single-beam spectrophotometer (Varian Corp.). Near-IR spectra were recorded using a PerkinElmer Lambda 19 UV–vis−NIR absorption spectrometer in the laboratory of the Chisholm research group at The Ohio State University. In each measurement, the sample was referenced to a matched cuvette containing pure solvent. To observe optically forbidden transitions in the near-IR region, samples with concentrations of $\sim$150 μM were employed. No aggregation phenomena were observed under such conditions.

Oscillator strengths, *f*, of the Q and near-IR absorption bands of the two complexes were estimated by fitting the experimental spectral bands with a single Gaussian function and using the expression

$$f = (3.32 \times 10^{-9}) \int e^{-(\Delta\nu/\theta)^2} \, d\nu = (3.32 \times 10^{-9})\sqrt{\pi}\epsilon_{max}\theta \quad (1)$$

where θ is the half-width at $\epsilon = \epsilon_{max}/e$. The width parameter θ is related to the full width (*h*) at half-maximum ($\epsilon_{max}/2$) by the expression $h = 2(\ln 2)^{1/2}\theta$.

The oscillator strengths obtained from eq 1 neglect the solvent refractive index correction. For common solvents, the inclusion of the refractive index correction may result in changes on the order of 10–20%.[21]

D. Luminescence Spectra. Steady-state near-IR luminescence spectra were obtained using a PTI Instruments QM-4/2006-SE spectrofluorimeter. Samples in a 10 mm $\times$ 10 mm path length quartz cuvette were excited using a 75 W Xe arc lamp excitation

source, and near-IR signals were monitored at the right-angle geometry using a Peltier-cooled InGaAs detector with lock-in amplification. Luminescence spectra were acquired at room temperature, and all solutions were saturated with Ar prior to luminescence experiments. Appropriate filters were used to prevent scattered light from entering the detection system. All of the spectra were corrected for the sensitivity of the detector.

The fluorescence quantum efficiency of CuNc(OBu)$_8$ was measured using ZnNc(OBu)$_8$ in toluene as a standard. The reference and the sample were excited at 458 nm, where they had the same absorbance ($A = 0.02$). The areas under the fluorescence spectra (*G*) were measured, and fluorescence quantum efficiencies (q_M) were calculated according to the equation

$$q_M^{sample} = \left(\frac{G_{sample}}{A_{sample}}\right)\left(\frac{A_{ZnNc(OBu)_8}}{G_{ZnNc(OBu)_8}}\right)q_M^{ZnNc(OBu)_8} \quad (2)$$

The value for the absolute fluorescence quantum efficiency for the Zn complex was estimated using the Strickler–Berg equation:[22]

$$\frac{1}{\tau_{rad}} = k_{rad} = 2.88 \times 10^{-9}\left(\frac{n_f^3}{n_a}\right)\langle \nu_f^{-3}\rangle^{-1}\int\frac{\epsilon \, d\nu}{\nu} \quad (3)$$

The calculated radiative lifetime was found to be $\sim$8.45 ns, in good agreement with the radiative lifetime of 8.8 ns for unsubstituted ZnNc measured in DMF.[23] The singlet-state lifetime of 0.6 ns measured using transient absorption spectrometry was employed to calculate a value of $q_M = 0.07$ for the absolute quantum efficiency of the Zn complex.

For the $^{2,4}T(\pi, \pi^*)$ near-IR emission measurements, Xe arc excitation (830 nm) was used and the concentration of naphthalocyanines was $\sim$6 μM, providing an optical absorbance of $\sim$1.2 in the Q-band maximum.

E. Ultrafast Pump–Probe Measurements. Details of the pump–probe instrument for ultrafast transient absorption measurements at the Ohio Laboratory for Kinetic Spectrometry at Bowling Green State University have been described previously.[24] Recent improvements to enhance signal-to-noise characteristics have been published elsewhere.[25] For the present measurements, the main part (95%) of the fundamental output beam (95 fs, 1 kHz, 800 nm) from an amplified, mode-locked Ti:sapphire laser (Hurricane, Spectra-Physics) was used to excite the sample or to pump an optical parametric amplifier (OPA 800, Spectra Physics). An OPA was used to generate excitation pulses in the range 800–900 nm (the second harmonic of the idler). The pump intensity was attenuated to give an energy of 1–3 μJ/pulse at the sample. The transient absorption signal was monitored with the white-light continuum probe in the 460–780 nm spectral range or with the extended to the near-IR continuum in the region of 800–1100 nm. The instrument response time of the ultrafast spectrometer was $\sim$200 fs. The concentrations of the naphthalocyanines were typically $\sim$20–30 μM in the 2 mm path length cuvette. Absorption spectra of the solutions were measured before and after the experiment to check for possible sample degradation.

F. Quantum Chemical Calculations. All of the calculations were performed with the ADF program package.[13,26] Geometry

(19) NiNc(OBu)$_8$ and CuNc(OBu)$_8$ are available commercially but were prepared in this study to assure the purity desired.

(20) Yang, S.; Liu, E.; Chen, N.; Huang, J.; Pu, P.; Duan, W.; Wu, Y. Q.; Zuo, X.; Mao, G. *Chin. J. Inorg. Chem.* **1997**, *13*, 83.

(21) McHugh, A. J.; Gouterman, M. *Theor. Chim. Acta* **1969**, *13*, 249.

(22) Strickler, S. J.; Berg, R. A. *J. Chem. Phys.* **1962**, *37*, 814.

(23) Kumar, G. A.; Santhosh, C. *Mater. Lett.* **2003**, *57*, 2315.

(24) Nikolaitchik, A. V.; Korth, O.; Rodgers, M. A. J. *J. Phys. Chem. A* **1999**, *103*, 7587.

(25) Pelliccioli, A. P.; Henbest, K.; Kwag, G.; Carvagno, T. R.; Kenney, M. E.; Rodgers, M. A. J. *J. Phys. Chem. A* **2001**, *105*, 1757.

(26) te Velde, G.; Bickelhaupt, F. M.; Baerends, E. J.; Fonseca Guerra, C.; van Gisbergen, S. J. A.; Snijders, J. G.; Ziegler, T. *J. Comput. Chem.* **2001**, *22*, 931.

optimizations and ground-state electronic structure calculations were performed using the Vosko−Wilk−Nusair (VWN) local density approximation (LDA) functional[27] plus the Becke88−Perdew86 (BP) generalized gradient approximation (GGA).[28,29] The spin-unrestricted DFT formalism was employed to examine the open-shell Co and Cu complexes. The model compounds $MNc(OMe)_8$ (M = Co, Cu; Me = methyl), in which the butyl substituents of the title compounds were replaced by methyl groups, were chosen in order to facilitate the calculations. Structure optimizations were performed using no constraints, starting from nonsymmetric structures in which methyl substituents residing on the same naphthoindole subunit had the same orientation as in $NiNc(OMe)_8$.[10] The structures of $CoNc(OMe)_8$ and $CuNc(OMe)_8$ were optimized by assuming an $S = ^1/_2$ spin state.

Excitation energies were calculated using ordinary (spin-unrestricted) TDDFT[11] and spin-unrestricted SF-TDDFT based on a noncollinear representation of the XC potential.[11,12] In ADF, the SF-TDDFT approach is implemented within the Tamm−Dancoff approximation (TDA).[30] In the TDDFT calculations, the same GGA as in the DFT calculations was used for the XC potential, which appears in the zeroth-order Kohn–Sham (KS) equations. Recent studies of the ground and excited states of cobalt[31−35] and nickel tetrapyrroles[10,36−38] have demonstrated that nonhybrid functionals, including the BP functional used in this study, provide results that are very consistent with experiment. For the so-called XC kernel, the first functional derivative of the time-dependent XC potential with respect to the time-dependent density $\rho(\mathbf{r}', t')$, the adiabatic local density approximation (ALDA) was employed.

Vertical absorption energies, E_{va}, were evaluated at the ground-state optimized geometry. For selected excited states, adiabatic energies, E_{adia}, were also computed according to the expression

$$E_{adia} = E_{ve} + \Delta E \qquad (4)$$

where E_{ve} is the vertical emission energy, which is calculated at the TDDFT level using the relaxed excited-state geometry. The ΔE term accounts for the change in energy of the ground state upon deformation to the relaxed geometry of the excited state (for a schematic definition of the calculated energies, see Figure 10 in ref 38).

The optimized ground- and excited-state structures were verified to represent local minima by calculation of harmonic frequencies. Spin contamination, monitored by the expectation value of S^2, was found to be negligible in all cases.

Effects of the solvent on the excitation energies were modeled with the conductor-like continuum solvent model (COSMO),[39−41]
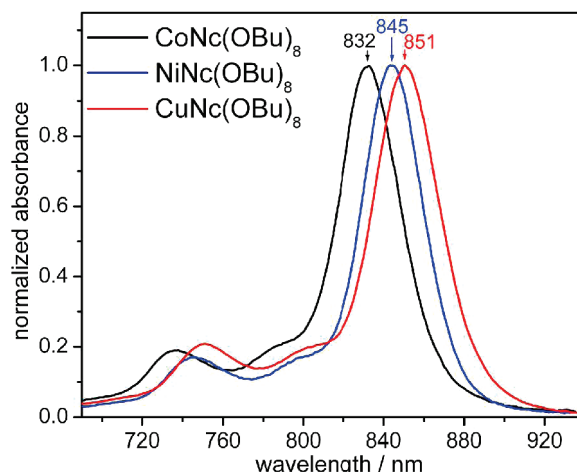
(27) Vosko, S. H.; Wilk, L.; Nusair, M. *Can. J. Phys.* **1980**, *58*, 1200.
(28) Becke, A. *Phys. Rev. A* **1988**, *38*, 3098.
(29) Perdew, J. P. *Phys. Rev. B* **1986**, *33*, 8822.
(30) Hirata, S.; Head-Gordon, M. *Chem. Phys. Lett.* **1999**, *314*, 291.
(31) Andruniow, T.; Kozlowski, P. M.; Zgierski, M. Z. *J. Chem. Phys.* **2001**, *115*, 7522.
(32) Andruniow, T.; Zgierski, M. Z.; Kozlowski, P. M. *J. Phys. Chem. A* **2002**, *106*, 1365.
(33) Kozlowski, P. M.; Andruniow, T.; Jarzecki, A. A.; Zgierski, M. Z.; Spiro, T. G. *Inorg. Chem.* **2006**, *45*, 5585.
(34) Kuta, J.; Patchkovskii, S.; Zgierski, M. Z.; Kozlowski, P. M. *J. Comput. Chem.* **2006**, *27*, 1429.
(35) Jaworska, M.; Lodowski, P.; Andruniow, T.; Kozlowski, P. M. *J. Phys. Chem. B* **2007**, *111*, 2419.
(36) Patchkovskii, S.; Kozlowski, P. M.; Zgierski, M. Z. *J. Chem. Phys.* **2004**, *121*, 1317.
(37) Rosa, A.; Ricciardi, G.; Baerends, E. J.; Zimin, M.; Rodgers, M. A. J.; Matsumoto, S.; Ono, N. *Inorg. Chem.* **2005**, *44*, 6609.
(38) Gunaratne, T. C.; Gusev, A. V.; Peng, X.; Rosa, A.; Ricciardi, G.; Baerends, E. J.; Rizzoli, C.; Kenney, M. E.; Rodgers, M. A. J. *J. Phys. Chem. A* **2005**, *109*, 2078.
(39) Klamt, A.; Schürmann, G. *J. Chem. Soc., Perkin Trans.* **1993**, *2*, 799.

Figure 1. Normalized ground-state absorption spectra of $CoNc(OBu)_8$, $NiNc(OBu)_8$, and $CuNc(OBu)_8$ in toluene solution in the Q-band region.

using the structures optimized in the gas phase. In the ADF implementation, COSMO surface charges are not explicitly considered in the TDDFT procedure other than through their influence on the ground-state density.[41] This effectively amounts to using the ground-state surface charges for both the ground and excited states as a first approximation to simulate the effects of the solvent on the excitation energies. The high-frequency component of the solvent electric susceptibility, which accounts for changes in the electronic structure of the solvent upon electronic excitations within the solute, was not considered.

The DFT and TDDFT calculations employed the all-electron ADF TZ2P basis set, which is an uncontracted triple-ζ STO basis set having one 3d and one 4f polarization function for each C, N, and O atom, one 2p and one 3d polarization function for each H atom, and a triple-ζ 3d, 4s basis with one 4p and one 4f function for Co and Cu.

Results and Discussion

A. Ground-State Absorption Spectra. The normalized ground-state absorption spectra of the cobalt(II) and copper(II) octabutoxynaphthalocyanine complexes in toluene in the energy window of the Q band are displayed in Figure 1. For comparison purposes, the optical absorption spectrum of the nickel(II) analog is also given. The complexes exhibited a very intense Q(0, 0) band in the 830–850 nm region with a weak vibrational progression toward the blue. The extinction coefficients of the Q(0, 0) band in toluene were 1.68×10^5 M^{-1} cm^{-1} (832 nm), 2.25×10^5 M^{-1} cm^{-1} (845 nm), and 2.31×10^5 M^{-1} cm^{-1} (851 nm) for the Co, Ni, and Cu complexes, respectively. Notably, the Q-band system experienced a clear red shift across the $MNc(OBu)_8$ (M = Co, Ni, Cu) series.

In addition to the strongly allowed transition to the Q state, $CoNc(Bu)_8$ and $CuNc(OBu)_8$ spectra exhibited weak bands in the near-IR region (Figure 2). The copper complex showed two distinct absorptions, one at 1155 nm ($\epsilon \approx 250$ M^{-1} cm^{-1}) and the other at 1440 nm ($\epsilon \approx 150$ M^{-1} cm^{-1}). On the basis of the emission data and TDDFT calculations (described below), these bands were assigned to the "tripdoublet", $^2T_1(\pi$,

(40) Klamt, A.; Jonas, V. *J. Chem. Phys.* **1996**, *105*, 9972.
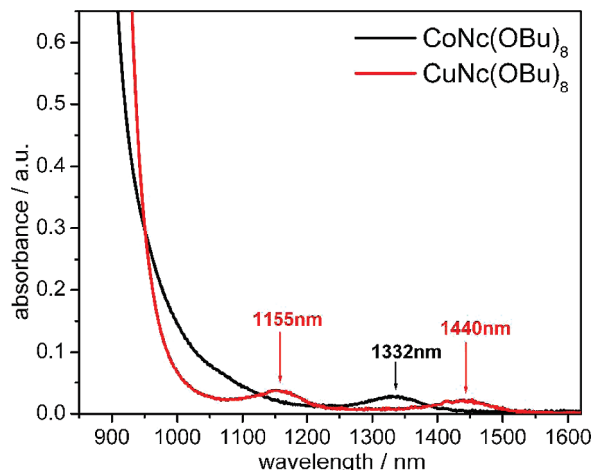(41) Pye, C. C.; Ziegler, T. *Theor. Chem. Acc.* **1999**, *101*, 396.

Figure 2. Near-IR ground-state absorption spectra of ~150 μM CoNc(OBu)$_8$ and CuNc(OBu)$_8$ in CH_2Cl_2.

π^*), and quartet, $^4T_1(\pi, \pi^*)$, excited states derived from the $\pi \rightarrow \pi^*$ transition between the highest-occupied and lowest-unoccupied Gouterman molecular orbitals (G-HOMO and G-LUMO, respectively). This transition also generates the "singdoublet", $^2S_1(\pi, \pi^*)$, excited state that accounts for the Q(0, 0) band.[42,43] As expected, the $^2T_1(\pi, \pi^*)$ state, which is weakly allowed, acquired more intensity than the $^4T_1(\pi, \pi^*)$ state. In the Co complex, however, only one weak absorption at 1332 nm ($\epsilon \approx 210$ M^{-1} cm^{-1}) could be resolved in the near-IR spectrum, although one or more absorptions are likely to contribute to the broadening of the red tail of the Q band (see Figure 2). TDDFT calculations suggested that the absorption at 1332 nm be assigned to the $^4T_1(\pi, \pi^*)$ excited state. Weak near-IR absorption bands have been reported for cobalt(II) and copper(II) phthalocyanines and assigned, mostly on the basis of emission data, to tripmultiplets.[44,45] Table 1 summarizes the absorption and emission properties of the complexes.

B. NIR Emission Spectra of Co(OBu)₈ and Cu(OBu)₈. The title compounds were examined for emission properties at room temperature. No fluorescence was observed for the cobalt complex, whereas CuNc(OBu)$_8$ was weakly fluorescent with an emission maximum at ~878 nm (the fluorescence spectrum was obtained using a monochromator slit width of 10 mm). The emission and absorption spectra of the Cu complex are brought together in Figure 3. The quantum efficiency for fluorescence of CuNc(OBu)$_8$ was estimated using the ZnNc(OBu)$_8$ complex as a standard; an approximate value for the absolute quantum efficiency of the Zn complex was obtained using the Strickler–Berg

equation (see Luminescence Spectra in the Experimental Section). The CuNc(OBu)$_8$ fluorescence quantum efficiency obtained in this way was ~3×10^{-4}, implying that effective nonradiative channels exist for deactivation of the Q state.

Upon excitation at 830 nm, a 6 μM solution of the copper complex in Ar-saturated benzene showed a clear luminescence band at 1457 nm, most likely due to emission from the $^4T(\pi, \pi^*)$ state. In addition, a poorly resolved shoulder in the fluorescence tail could be seen at around 1175 nm. It was tempting to assign this feature to emission from the $^2T_1(\pi, \pi^*)$ state, although, in view of its weakness, the emission might arise from the presence of emissive impurities.

Under the same experimental conditions, the cobalt complex did not show the $^2S_1 \rightarrow {}^2S_0$ fluorescence signal. However, a weak emission band at 1092 nm, presumably from the $^2T_1(\pi, \pi^*)$ state, could be resolved upon excitation of the complex in Ar-saturated benzene at 830 nm (not shown); in the near-IR absorption spectrum of CoNc(OBu)$_8$, this band was hidden in the Q-band absorption tail.

C. Transient Absorption Experiments. Femtosecond transient absorption spectrometry with excitation wavelengths within the Q bands (800–845 nm) was employed to investigate the deactivation of the excited states of the Co(II) and Cu(II) naphthalocyanine complexes. The transient absorption species formed were probed in the visible and near-IR regions.

CuNc(OBu)₈. Figure 4 shows transient absorption spectra for CuNc(OBu)$_8$ in toluene (35 μM) at different time delays following excitation at 800 nm and probed in the visible (Figure 4a) and near-IR (Figure 4b) regions of the spectrum. The first observed transient in the visible region (3 ps) displayed features characteristic of excited states localized on phthalocyanine and naphthalocyanine macrocycles,[10,16,24,38,46–50] exhibiting a broad positive absorption band with a maximum at 635 nm and two negative bands, at 480 and 755 nm, arising from ground-state depopulation. During the first picosecond or so, the positive absorption signal at ~650 nm was seen to grow (see Figure 4a, inset). As the time delay between pump and probe was further increased, the intensity of the transient absorption signal decreased but no changes in its spectral shape were detected. Two isosbestic points connecting the positive and negative features, one at 510 nm and the other at 740 nm, were maintained during the decay. In the near-IR region, the only observed spectral feature was bleaching in the Q-band region caused by ground-state depopulation; no spectral shift was detected during the time window of the experiment.

Time profiles at 680 and 850 nm are shown in panels a and b of Figure 5, respectively. The profiles are truncated by the limit of the experimental time window. They were

(42) The classification of the (π, π^*) excited states in terms of "singdoublets" and "tripdoublets" was originally introduced by Gouterman and co-workers (see ref 43). Interaction between the $^1(\pi, \pi^*)$ states of the macrocycle and the unpaired d electron on the metal produces doublet states (singdoublets), while interaction between the $^3(\pi, \pi^*)$ states of the macrocycle and the unpaired d electron yields doublets (tripdoublets) and quartets.

(43) Gouterman, M.; Mathies, R. A.; Smith, B. E.; Caughey, W. S. *J. Chem. Phys.* **1970**, *52*, 3795.

(44) Vincett, P. S.; Voigt, E. M.; Rieckhoff, K. E. *J. Chem. Phys.* **1971**, *55*, 4131.

(45) Lever, A. B. P.; Pickens, S. R.; Minor, P. C.; Licoccia, S.; Ramaswamy, B. S.; Magnell, K. *J. Am. Chem. Soc.* **1981**, *103*, 6800.

(46) Nikolaitchik, A. V.; Rodgers, M. A. J. *J. Phys. Chem. A* **1999**, *103*, 7597.

(47) Aoudia, M.; Cheng, G.; Kennedy, V. O.; Kenney, M. E.; Rodgers, M. A. J. *J. Am. Chem. Soc.* **1997**, *119*, 6029.

(48) Firey, P. A.; Ford, W. E.; Sounik, J. R.; Kenney, M. E.; Rodgers, M. A. J. *J. Am. Chem. Soc.* **1988**, *110*, 7626.

(49) Rihter, B. D.; Kenney, M. E.; Ford, W. E.; Rodgers, M. A. J. *J. Am. Chem. Soc.* **1990**, *112*, 8064.

(50) Fournier, M.; Pepin, C.; Houde, D.; Ouellet, R.; Van Lier, J. E. *Photochem. Photobiol. Sci.* **2004**, *3*, 120.

Table 1. Absorption and Emission Data for CoNc(OBu)$_8$ and CuNc(OBu)$_8$

	absorption λ_{max} [nm] (ϵ [M^{-1} cm^{-1}])			emission λ_{max} [nm] (ϕ [%])		
CoNc(OBu)$_8$	832 (1.68 × 10^5)^a	n/a	1332 (210)^b	−	1092^d	−
CuNc(OBu)$_8$	851 (2.31 × 10^5)^a	1155 (250)^b	1440 (150)^b	878 (0.03)^c	1172^e	1460^d

^{a} Measured in toluene at room temperature. ^{b} Measured in CH$_2$Cl$_2$ at room temperature. ^{c} Measured in Ar-saturated benzene at room temperature with λ_{exc} = 458 nm. ^{d} Measured in Ar-saturated benzene at room temperature with λ_{exc} = 830 nm. ^{e} Seen as a shoulder in the red tail of the fluorescence emission.

fitted to a zero baseline using a single-exponential function, providing a lifetime of ∼1.1 ns.

Figure 6 displays the rise time of the 630 nm transient superimposed on the time profile of a solvent-derived Raman signal that shows the instrument response profile. As can be seen, the increase in the transient absorption at 630 nm occurs more slowly than the ∼200 fs solvent response. Experimental points were fitted starting from the time when the Raman signal disappeared, leading to an estimate of 200 fs for the rise time of the 630 nm absorption.

CoNc(OBu)$_8$. Figure 7a shows overlaid transient absorption spectra in the visible region at a series of delay times after excitation of CoNc(OBu)$_8$ in toluene (23 μM) using 832 nm pulses. Formation of the positive absorption band and the ground-state bleaching was complete within the instrument response time (∼200 fs). The first observed transient in the visible region (at 1.2 ps in Figure 7a) revealed spectral features similar to those reported above for CuNc(OBu)$_8$ and previously[10] for NiNc(OBu)$_8$, i.e., a broad positive absorption centered at 650 nm and negative absorption bands at 470 and 745 nm arising from ground-state bleaching.

Figure 7b shows a series of time-delayed spectra in the near-IR region. In addition to the negative-absorption spectral feature arising from bleaching of the Q band, the spectrum of the first observed transient was also characterized by a broad positive absorption to the red of the bleaching maximum.
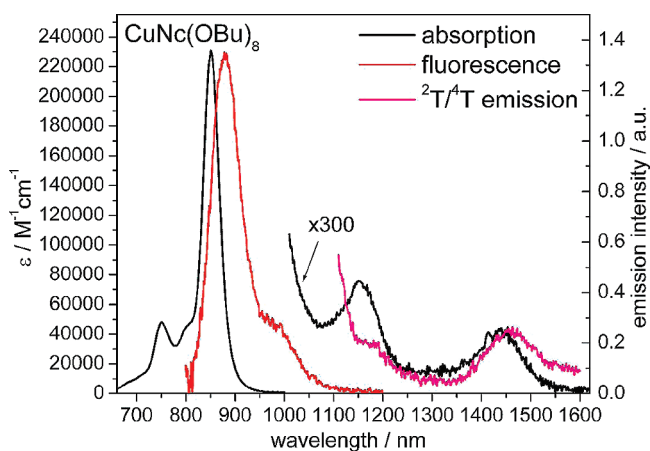
As time progressed, the featureless positive absorption in the visible region decayed to a zero baseline, while the negative bands became blue-shifted during the decay period. Eventually, a spectral transient with alternating negative and positive lobes at 735 and 765 nm, characteristic of a (d, d) state, remained (Figure 7a, inset). In Figure 7b, the blue shift of the transient spectrum is more obvious. As can be seen, during the first 5 ps, both the negative absorption extreme and the broad positive absorption band at ∼900 nm shifted toward the blue and narrowed significantly. During this time, the difference spectrum evolved into one having a derivative-like shape, and no isosbestic behavior was observed. At later times, the derivative-shaped spectrum decayed uniformly to the baseline, reflecting complete ground-state recovery. The inset in Figure 7a shows an isosbestic point near 755 nm,
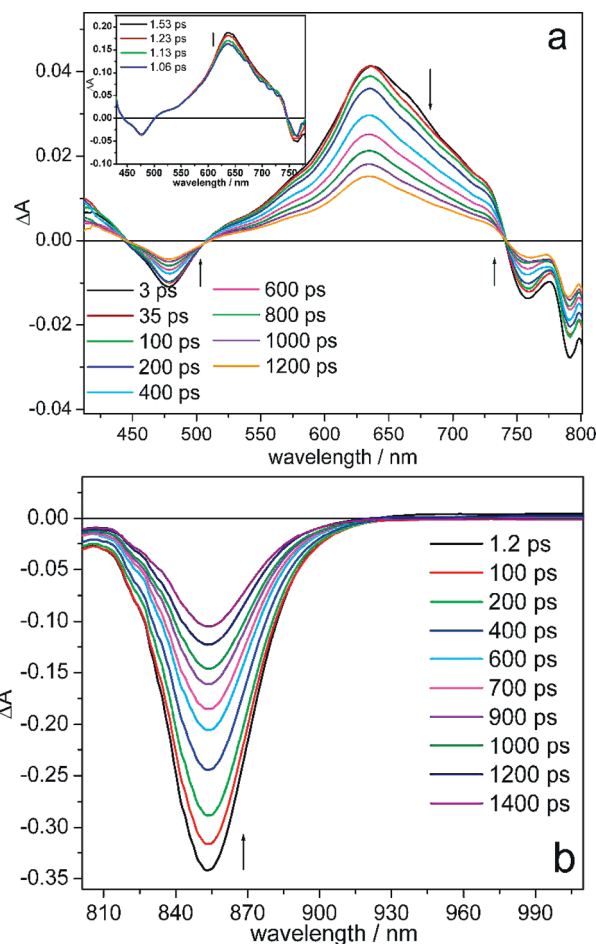

Figure 3. Ground-state absorption spectra (black lines) and static emission spectra (red and pink lines) of CuNc(OBu)$_8$. Ground-state absorption spectra were measured in toluene (Q-band region) and CH$_2$Cl$_2$ (near-IR region). Emission spectra were obtained in Ar-saturated benzene with excitation wavelengths of 458 nm (fluorescence emission) and 830 nm (near-IR emission). Concentrations of ∼0.5 μM [$A_{Q(0,0)}$ = 0.12] and ∼6 μM were used for the fluorescence and near-IR emission measurements, respectively. The fluorescence spectrum was normalized to the Q-band absorption maximum, and the near-IR emission spectrum was normalized to the maximum of the lowest-energy absorption band (1440 nm).

Figure 4. Evolution of the transient absorption spectra of CuNc(OBu)$_8$ in toluene (∼35 μM) upon photoexcitation at 800 nm using a pump energy of 5 μJ/pulse. (a) Transient absorption spectra probed in the visible region. Inset: transient absorption evolution showing growth of the positive feature during the first picosecond of the experiment. (b) Transient absorption spectra probed in the near-IR region at various delay times.
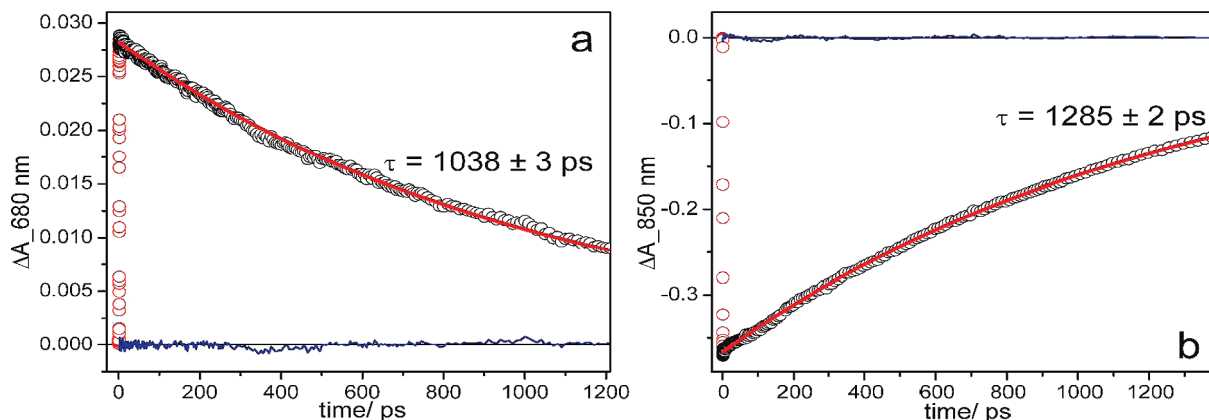
Figure 5. Kinetic profiles of the transient absorption signals at probe wavelengths of (a) 680 and (b) 850 nm for CuNc(OBu)$_8$ in toluene after excitation at 800 nm. The red lines are fits to the experimental data points and blue lines are residuals for the fits.
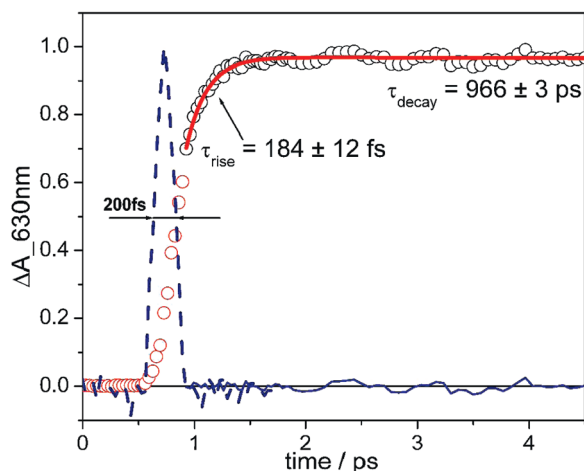

Figure 6. Kinetic profile of the transient absorption of CuNc(OBu)$_8$ in toluene solution at 630 nm. The blue dashed curve is the instrument response to a solvent Raman signal (~200 fs). Both traces are normalized to unity to demonstrate the differences in response time.

indicating concomitant behavior of the decay of the positive absorption and the ground-state repopulation.

The spectral evolution described above was accompanied by complex temporal behavior having wavelength-dependent lifetimes. Temporal decay profiles recorded at 650 and 900 nm are shown in panels a and b of Figure 8, respectively. The positive absorption in the visible region (Figure 8a) decayed to a zero baseline with single-exponential behavior having a lifetime of 1.0 ps, which showed no wavelength dependence between 500 and 700 nm. The signal monitored at 900 nm (Figure 8b) was best fitted by the sum of a rise having a lifetime of $\tau_1 = 518 \pm 16$ fs and a double-exponential decay having lifetimes of $\tau_2 = 1.57$ and $\tau_3 = 14.7$ ps. Careful scrutiny of the lifetimes of the time profiles beyond 700 nm indicated that the first two lifetimes decreased as the wavelength increased within each of the spectral envelopes separated by the isosbestic point, with ranges of 0.3−0.8 and 1.4−3.6 ps for τ_1 and τ_2, respectively.

D. Theoretical Studies of the Ground and Excited States. Molecular and Electronic Structure. Geometry optimizations were performed with no symmetry constraints, starting from nonsymmetric structures in which methyl substituents residing on the same naphthoindole subunit had the same orientation as in NiNc(OMe)$_8$.[10] Consistent with

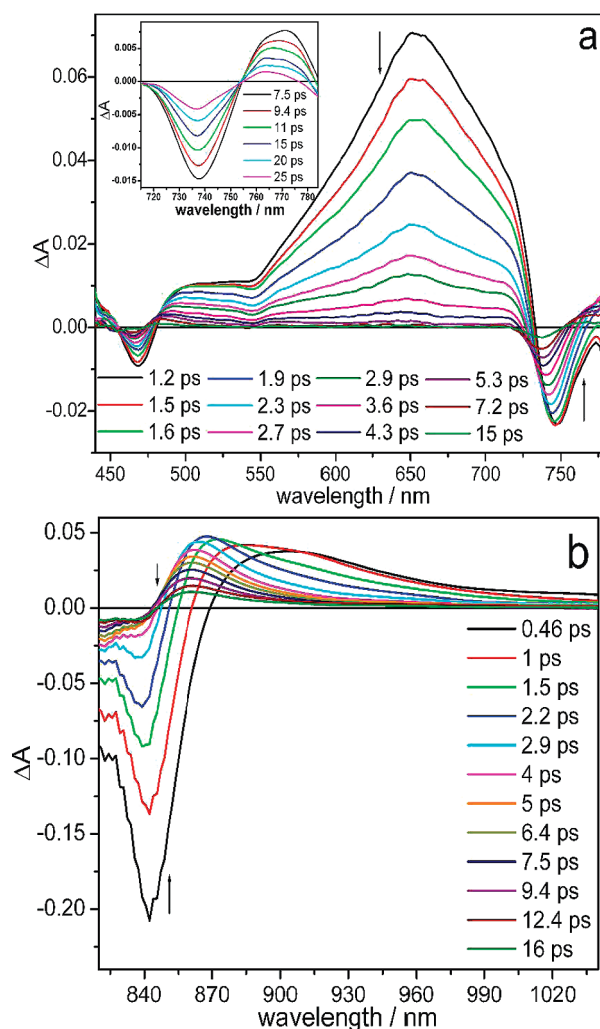**Figure 7.** Evolution of the transient absorption spectra of CoNc(OBu)$_8$ in toluene (~23 μM). (a) Transient absorption spectra in the visible region following photoexcitation at 832 nm using a pump energy of 1 μJ/pulse. Inset: enlarged area of the transient absorption evolution at times later in the decay, showing isosbestic behavior. (b) Transient absorption spectra in the near-IR region following excitation at 800 nm.

the results of magnetic and electron paramagnetic resonance (EPR) experiments showing that Co(II) and Cu(II) phthalocyanines contain one unpaired electron,[51–54] the structures

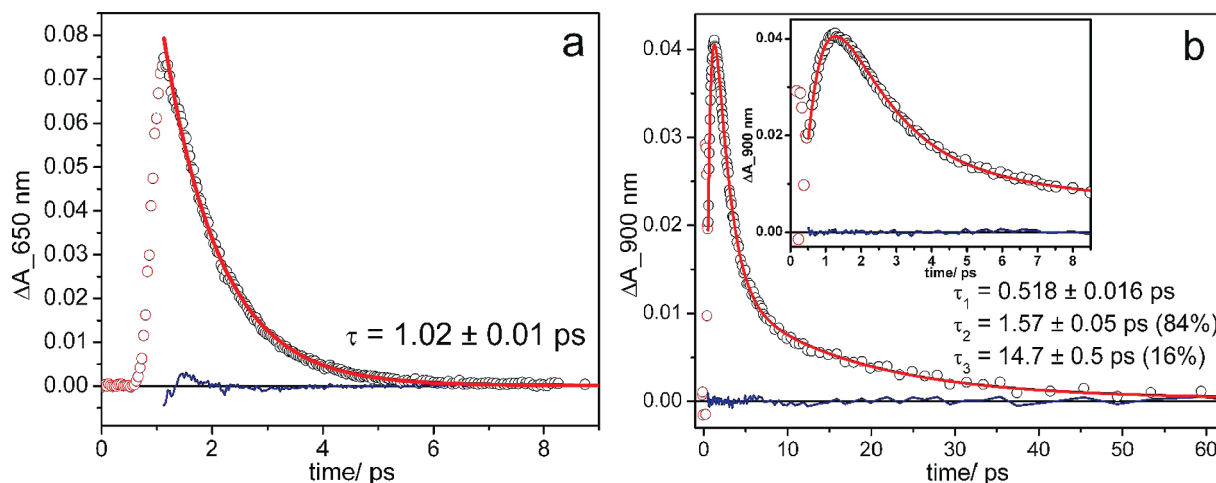(51) Assour, J. M.; Kahn, W. K. *J. Am. Chem. Soc.* **1965**, *87*, 207.

Figure 8. Kinetic behavior of transient absorption signals for CoNc(OBu)$_8$ in toluene after excitation at 832 nm using probe wavelengths of (a) 650 and (b) 900 nm. Solid red lines are fits to the experimental data points.
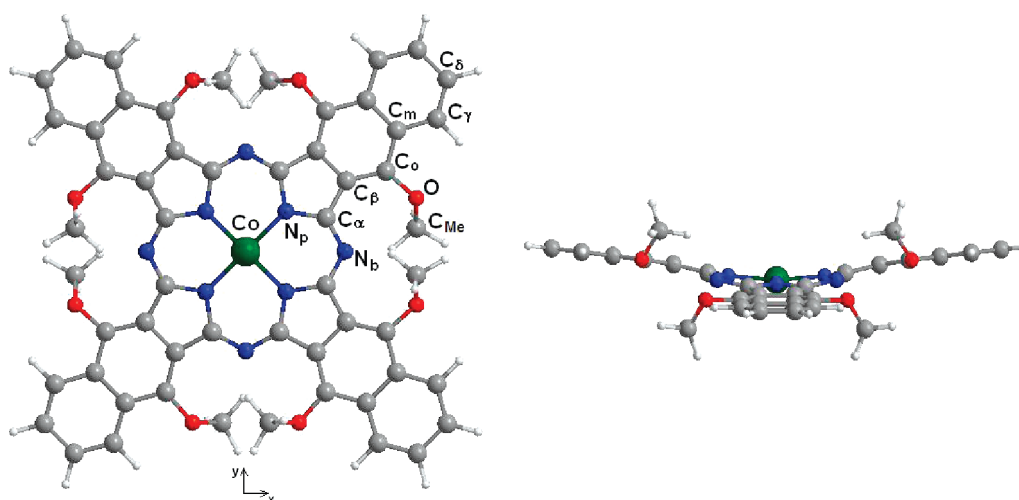

Figure 9. Top view (left) and side view (right) of the DFT-optimized molecular structure of CoNc(OMe)$_8$.

of CoNc(OMe)$_8$ and CuNc(OMe)$_8$ were optimized by assuming an $S = \frac{1}{2}$ spin state. In both cases, the system evolved toward a symmetric structure with D_{2d} symmetry (see Figure 9). The calculated ground states of the cobalt and copper complexes were $^2A_1$ and $^2B_2$, respectively. The most relevant structural parameters calculated for CoNc(OMe)$_8$ and CuNc(OMe)$_8$ are gathered in Table 2 along with those previously obtained for NiNc(OMe)$_8$.[10]

Similar to the nickel analog, CoNc(OMe)$_8$ and CuNc(OMe)$_8$ have a saddled structure in which the methyl groups are displaced from the plane of the pertinent naphthoindole moiety. The dihedral angle between adjacent pyrrole ring planes, $(C_\alpha-N_p-N_p-C_\alpha)_{ad}$, which defines the degree of saddling of the macrocycle, is virtually the same ($\sim 11°$) in all three complexes. The torsion angle $C_{Me}-O-C_o-C_b$, which provides a measure of the displacement of the C_{Me} atoms from the indole plane, is also substantially insensitive to the nature of the coordinated metal. This is in line with the tilting of the methyl groups out of the mean naphthalo-

Table 2. Selected Bond Lengths (Å), Bond Angles (deg), and Metrical Parameters Calculated for MNc(OMe)$_8$ (M = Co, Ni, Cu)

	Co	Ni[a]	Cu
M−N$_p$	1.920	1.906	1.964
C$_\alpha$−N$_p$	1.381	1.381	1.374
C$_\alpha$−C$_\beta$	1.453	1.453	1.458
C$_\beta$−C$_\beta$	1.432	1.430	1.436
C$_o$−O	1.368	1.368	1.368
C$_\alpha$−N$_b$	1.322	1.320	1.327
C$_\alpha$−N$_p$−C$_\alpha$	107.9	107.6	109.3
C$_\alpha$−N$_b$−C$_\alpha$	122.8	122.2	124.1
O···O	3.880	3.865	3.911
C$_{Me}$−O−C$_o$−C$_\beta$	63.1	63.0	63.0
$(C_\alpha-N_p-N_p-C_\alpha)_{ad}$[b]	11.2	11.3	11.3

[a] Data taken from ref 10. [b] Dihedral angle (deg) between adjacent pyrrole ring planes.

cyanine plane being dictated by the necessity to minimize the steric hindrance between the $C_{Me}-H$ and $C_\gamma-H$ σ bonds. According to the data in Table 2, the M−N$_p$ distance changes significantly along the series. The trend in the calculated M−N$_p$ distances, Co−N$_p$ (1.920 Å) > Ni−N$_p$ (1.906 Å) < Cu−N$_p$ (1.964 Å), is consistent with that observed in the corresponding phthalocyanines[55–57] and, in the case of the

(52) Lever, A. B. P. *J. Chem. Soc.* **1965**, 1821.
(53) Chen, I.; Abkowitz, M.; Sharp, H. *J. Chem. Phys.* **1969**, *50*, 2237.
(54) Guzy, C. M.; Raynor, J. B.; Symons, M. C. R. *J. Chem. Soc.* **1969**, 2299.

(55) Williams, G. A.; Figgis, B. N.; Mason, R.; Mason, S. A.; Fielding, P. E. *J. Chem. Soc., Dalton Trans.* **1980**, 1688.
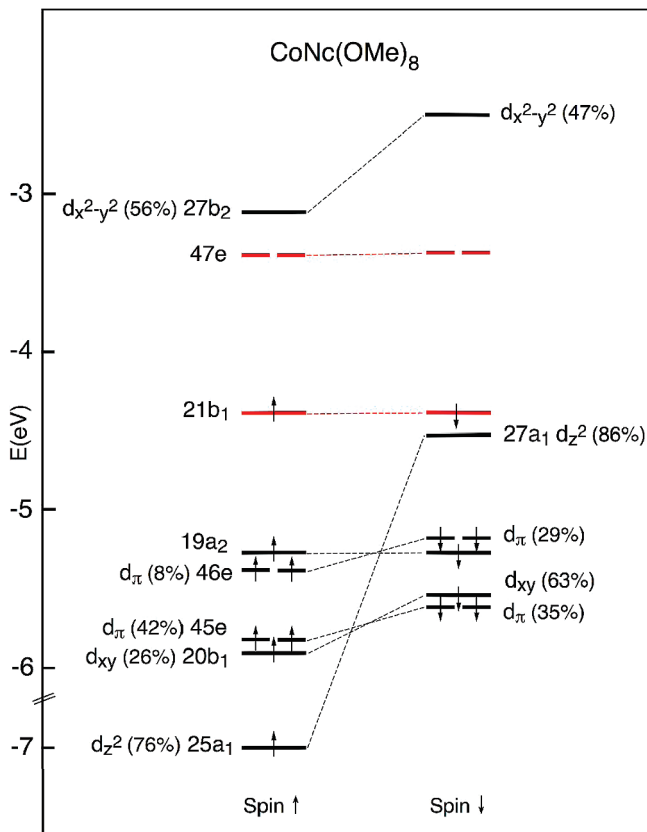
Figure 10. Energy-level scheme for CoNc(OMe)₈ obtained from spin-unrestricted DFT-BP/TZ2P calculations. In the numbering of the MOs, the core electrons (1s for C, N, and O; 1s–2p for Co) are not included. The Co 3d contributions to the spin orbitals are indicated in parentheses. The 21b₁ and 47e Gouterman MOs are indicated with red lines.

Figure 11. Spin density distribution in (a) CoNc(OMe)₈ and (b) CuNc(OMe)₈.

last two members of the series, naphthalocyanines.[58] If the shortening of the M−N$_p$ bond length in going from Co to Ni reflects the decrease of the ionic radius of the central metal, the "anomalously" long M−N$_p$ bond length in CuNc(OMe)₈ has to be traced to single occupancy of the σ antibonding molecular orbital (MO) formed from the Cu 3d$_{x^2−y^2}$ and N$_p$ lone-pair orbitals (discussed below). In response to the lengthening of the M−N$_p$ distance, a significant expansion of the macrocycle core occurs, as evidenced by the increases in the C$_\alpha$−N$_b$ bond distance and the C$_\alpha$−N$_p$−C$_\alpha$ and C$_\alpha$−N$_b$−C$_\alpha$ bond angles relative to those in the nickel and cobalt analogs (Table 2).

An energy-level scheme showing the highest-occupied and lowest-unoccupied Kohn–Sham spin orbitals of CoNc(OMe)₈ is displayed in Figure 10. According to the DFT results, the unpaired electron resides in the 25a₁↑ spin orbital whose spatial part is mainly a pure metal orbital, largely 3d$_{z^2}$ (76%) with some 4s character (9%). Analysis of the electron density distribution in the complex indicates that the spin density is mostly located on the cobalt atom, with small pockets of opposite spin found on the N$_p$ atoms [see Figure 11a for a plot of the spin density distribution in CoNc(OMe)₈]. This is quite similar to what has been found in the case of
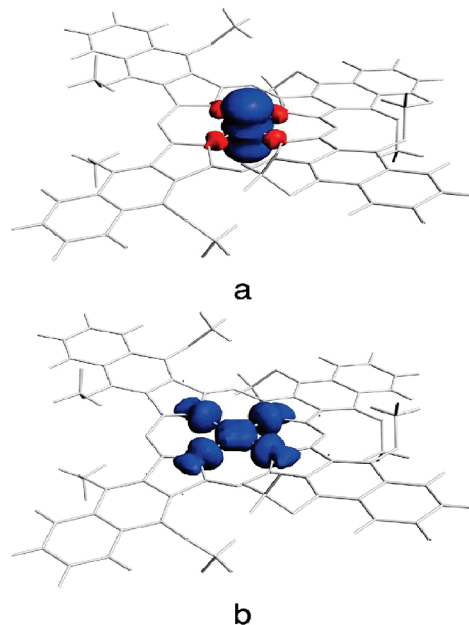
CoPc.[59,60] As expected for highly localized orbitals, the spin-down counterpart of the 25a₁↑ spin orbital, 27a₁↓, lies much (∼2.5 eV) higher in energy, just below the substantially unsplit 21b₁ G-HOMO. The Co 3d contributions to the spin orbitals indicate that among those shown in Figure 10, the 45e(d$_\pi$), 20b₁(d$_{xy}$), and 27b₂(d$_{x^2−y^2}$) MOs also involve the metal to a significant extent (it should be noted that we identified the metal 3d orbital pointing to the pyrrolic nitrogens as d$_{x^2−y^2}$, although, according to the D$_{2d}$ choice of axes, it is d$_{xy}$). The doubly degenerate 45e MO results from out-of-plane π interactions between the Co 3d$_\pi$ orbitals and occupied N$_p$-based π orbitals of the macrocycle. Notably, a sizable (29%) Co 3d$_\pi$ contribution is also found in the spin-down component of the higher-lying 46e orbital. The Co 3d$_\pi$ also contributes to some extent (5%) to the nearly unsplit 47e G-LUMOs. The 45e, 46e, and 47e MOs all have metal–ligand antibonding character. The 20b₁ MO results from an in-plane π antibonding interaction between the Co 3d$_{xy}$ orbital and a ligand orbital that is an N$_b$ lone-pair orbital with some in-plane N$_p$ p$_\pi$ character. The unoccupied 27b₂(d$_{x^2−y^2}$) MO is an antibonding Co−N$_p$ orbital composed of almost equal amounts of Co 3d$_{x^2−y^2}$ and pyrrolic nitrogen lone-pair orbitals.

According to the energy-level scheme in Figure 12, the 27b₂(d$_{x^2−y^2}$)↑ spin orbital becomes singly occupied in CuNc(OMe)₈. Consistent with the fact that the SOMO (singly occupied molecular orbital) is a nearly 50:50 mixture of Cu 3d$_{x^2−y^2}$ and N$_p$ lone pair orbitals, the spin density in the complex is almost equally distributed between the copper atom and the pyrrolic nitrogens [see Figure 11b for a plot of the spin density distribution in CuNc(OMe)₈]. A similar spin density distribution was found in CuPc.[53,54] The metal levels are significantly stabilized in going from the cobalt

(56) Schramm, C. J.; Scaringe, R. P.; Stojakovic, D. R.; Ibers, J. A.; Marks, T. J. *J. Am. Chem. Soc.* **1980**, *102*, 6702.
(57) Brown, C. J. *J. Chem. Soc. A* **1968**, 2488.
(58) Morishige, K.; Araki, K. *J. Chem. Soc., Dalton Trans.* **1996**, 4303.

(59) Figgis, B. N.; Kuckarski, E. S.; Reynolds, P. A. *J. Am. Chem. Soc.* **1989**, *111*, 1683.
(60) Bialek, B.; Kim, I. G.; Lee, J. I. *Thin Solid Films* **2006**, *513*, 110.
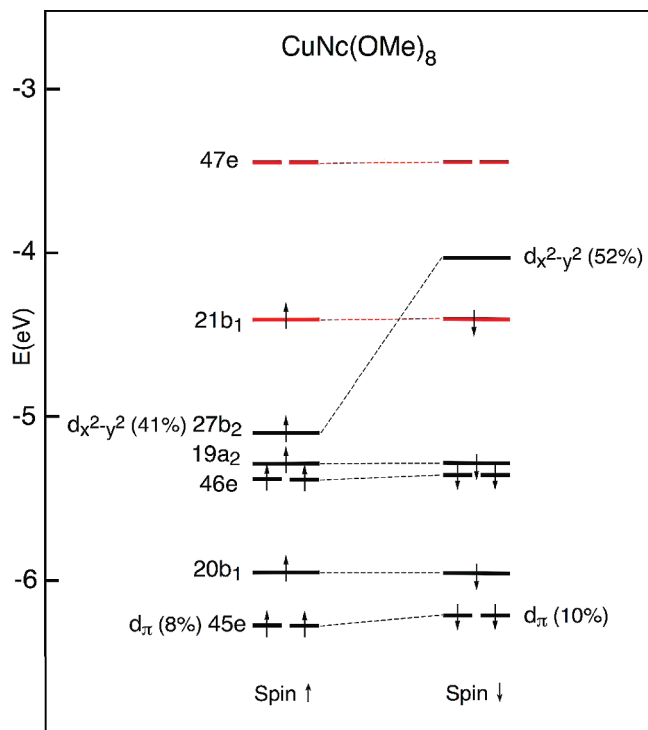
Figure 12. Energy-level scheme for CuNc(OMe)$_8$ obtained from spin-unrestricted DFT/BP/TZ2P calculations. In the numbering of the MOs, the core electrons (1s for C, N, and O; 1s–2p for Cu) are not included. The Cu 3d contributions to the spin orbitals are indicated in parentheses. The 21b$_1$ and 47e Gouterman MOs are indicated with red lines.

to the copper complex as a result of the increased nuclear charge of the metal. As a consequence, in CuNc(OMe)$_8$ there are no metal states in the upper valence region apart from the just-mentioned 27b$_2$(d$_{x^2-y^2}$) MO.

Excited States Below the $^2S_1(\pi, \pi^*)$ State. To gain insight into the deactivation mechanism of the $^2S_1(\pi, \pi^*)$ excited state in CoNc(OBu)$_8$ and CuNc(OBu)$_8$, the nature and energy of the excited states lying vertically between the $^2S_1(\pi, \pi^*)$ state and the ground state were explored theoretically. The molecules studied here have doublet ground states, leading to doublet and quartet excited states. One-electron transitions from fully occupied orbitals to virtual orbitals result in one set of quartet excited states and two sets of doublet states, whereas one-electron transitions from or into the singly occupied orbital result in doublet states.

As the photophysical experiments were performed in toluene solution, and, in the case of the copper complex, also in benzonitrile solution, the effects of the solvent on the excitation energies were also explored.

Vertical excitation energies (E_{va}) calculated for the lowest doublet and quartet states of CuNc(OMe)$_8$ and CoNc(OMe)$_8$ are gathered in Tables 3 and 4, respectively. Tables 3 and 4 also include adiabatic energies (E_{adia}) calculated for selected excited states and the composition of the BP/ALDA solution vectors in terms of the major one-electron MO transitions. The TDDFT energies of the excited states in the gas phase will be considered first, and then the solvent effects will be examined.

CuNc(OBu)$_8$. On the basis of the calculated vertical excitation energies and oscillator strengths, the intense Q(0, 0)

band, with a maximum at 852 nm and an oscillator strength of 0.690, was assigned to the 3^{2}E state, which was computed to lie at 1.37 eV (905 nm), in satisfactory agreement with experiment. This state is an almost pure G-21b$_1 \rightarrow$ G-47e, $\pi \rightarrow \pi^*$ state. The compositions of the excited states given in Table 3 indicate that the lower-lying 1^{2}E and 1^{4}E states originate from the same transition. Following the Gouterman notation,[43] the 3^{2}E, 1^{2}E, and 1^{4}E states will hereafter be designated $^2S_1(\pi, \pi^*)$, $^2T_1(\pi, \pi^*)$, and $^4T_1(\pi, \pi^*)$, respectively. According to the computed vertical excitation energies in Table 3, the $^2T_1(\pi, \pi^*)$ and $^4T_1(\pi, \pi^*)$ states were the best candidates for assignment to the weak absorptions appearing at 1155 and 1445 nm, respectively, in the near-IR spectrum of CuNc(OBu)$_8$ (see Figure 2). There was good agreement between the calculated excitation energies and the experimental band maxima, although the $^2T_1$/$^4T_1$ splitting was somewhat underestimated theoretically. In addition to the $^2T_1(\pi, \pi^*)$ and $^4T_1(\pi, \pi^*)$ states, TDDFT calculations in the gas phase also located three LMCT excited states below the $^2S_1(\pi, \pi^*)$ state. Two of these, the nearly degenerate 2^{2}E and 1^{2}A$_2$ states, vertically lie immediately below $^2S_1(\pi, \pi^*)$; the third one, 1^{2}B$_1$, with a computed energy of 0.38 eV, is the lowest-energy excited state. The LMCT excited states involve transitions from a π orbital of the macrocycle into the 27b$_2\downarrow$ spin orbital, a σ antibonding MO formed from the Cu 3d$_{x^2-y^2}$ and N$_p$ lone-pair orbitals. In regard to the LMCT states, it should be pointed out that our classification of LMCT states is based merely on the character of the MOs involved in the transitions. In fact, no net charge transfer from the ligand to the metal occurs; only a reorganization of the electronic density takes place. This happens quite frequently in so-called LMCT states of transition-metal complexes, including metallophthalocyanines[10,38] (for an extensive discussion on this topic, see ref 61). Therefore, the well-known failure of TDDFT to correctly predict the excitation energies of charge-transfer states[62–65] does not occur here, and the TDDFT energies calculated for the LMCT states can be trusted.

The pattern of excited states derived from the vertical excitation energies may be altered to some extent after consideration of geometry-relaxation effects. Detailed theoretical investigations of the excited-state properties of several nickel tetrapyrroles have clearly demonstrated that when geometric relaxation of the excited states is taken into account, the excitation energies of (d, d) and LMCT transitions involving population of the strongly antibonding σ Ni(d$_{x^2-y^2}$)−N$_p$(lone pairs) MO are shifted downward significantly (0.13–0.54 eV).[10,37,38] The π, π^* excited states, on the other hand, do not show significant relaxation, although they undergo Jahn–Teller distortion. The adiabatic excitation energies of the π, π^* states were indeed predicted

(61) Rosa, A.; Ricciardi, G.; Gritsenko, O.; Baerends, E. J. *Struct. Bonding (Berlin)* **2004**, *112*, 49.
(62) Casida, M. E.; Gutierrez, F.; Guan, J.; Gadea, F.-X.; Salahub, D.; Daudey, J.-P. *J. Chem. Phys.* **2000**, *113*, 7062.
(63) Dreuw, A.; Weisman, J. L.; Head-Gordon, M. *J. Chem. Phys.* **2003**, *119*, 2943.
(64) Dreuw, A.; Head-Gordon, M. *J. Am. Chem. Soc.* **2004**, *126*, 4007.
(65) Gritsenko, O.; Baerends, E. J. *J. Chem. Phys.* **2004**, *112*, 655.

Table 3. Excitation Energies of the Lowest Excited States of CuNc(OMe)$_8$

state[a]	composition[a] (%)	type	gas-phase		toluene/benzonitrile		exptl
			E_{va} (eV)[b]	E_{adia} (eV)	E_{va} (eV)[b]	E_{adia} (eV)	E (nm/eV)[b]
3^2E	$21b_1\uparrow \rightarrow 47e\uparrow$ (45) $21b_1\downarrow \rightarrow 47e\downarrow$ (49)	π, π^*	1.37 (0.662)		1.37/1.38 (0.698/0.701)		851/1.46 (0.690)[c] Q(0, 0)
2^2E	$46e\downarrow \rightarrow 27b_2\downarrow$ (100)	LMCT	1.33 (0.0001)		1.43/1.50 (0.0001/0.1740)		
1^2A_2	$19a_2\downarrow \rightarrow 27b_2\downarrow$ (100)	LMCT	1.27	1.10[d]	1.37/1.46	1.20[e]/1.29[e]	
1^2E	$21b_1\uparrow \rightarrow 47e\uparrow$ (52) $21b_1\downarrow \rightarrow 47e\downarrow$ (48)	π, π^*	0.91 (0.0003)		0.91/0.92 (0.0003)		1155/1.07 (0.0008)[f]
1^4E	$21b_1\downarrow \rightarrow 47e\uparrow$ (100)	π, π^*	0.89		0.90/0.90		1440/0.86 (0.0005)[f]
1^2B_1	$21b_1\downarrow \rightarrow 27b_2\downarrow$ (100)	LMCT	0.38	0.25[d]	0.48/0.57	0.33[e]/0.40[e]	

[a] Numbering and composition of the excited states refer to TDDFT calculations in the gas phase. [b] Oscillator strengths in parentheses. [c] In toluene solution, from this work. [d] Geometry optimization of the excited-state structure was performed under the constraint of D_{2d} symmetry. [e] Computed at the geometry optimized in the gas phase (D_{2d} symmetry). [f] In CH₂Cl₂ solution, from this work.

Table 4. Excitation Energies of the Lowest Excited States of CoNc(OMe)$_8$

state[a]	composition[a] (%)	type	gas-phase		toluene		exptl
			E_{va} (eV)[b]	E_{adia} (eV)	E_{va} (eV)[b]	E_{adia} (eV)	E (nm/eV)[b]
4^2E	$21b_1\uparrow \rightarrow 47e\uparrow$ (45) $21b_1\downarrow \rightarrow 47e\downarrow$ (49)	π, π^*	1.39 (0.662)		1.39 (0.660)		832/1.49 (0.540)[c] Q(0, 0)
2^2A_2	$21b_1\uparrow \rightarrow 27b_2\uparrow$ (100)	LMCT	1.27		1.31		
1^4A_2	$21b_1\downarrow \rightarrow 27b_2\uparrow$ (100)	LMCT	1.26		1.30		
1^2B_1	$20b_1\downarrow \rightarrow 27a_1\downarrow$ (100)	d_{xy}, d_{z^2}	1.20		1.24		
3^2E	$45e\downarrow \rightarrow 27a_1\downarrow$ (99)	LMCT/(d_π, d_{z^2})	1.02 (0.00003)		1.15 (0.0002)		
2^2E	$21b_1\uparrow \rightarrow 47e\uparrow$ (52) $21b_1\downarrow \rightarrow 47e\downarrow$ (47)	π, π^*	0.95 (0.0006)		0.96 (0.0006)		
1^4E	$21b_1\downarrow \rightarrow 47e\uparrow$ (100)	π, π^*	0.93		0.94		1332/0.93 (0.0006)[d]
1^2A_2	$19a_2\downarrow \rightarrow 27a_1\downarrow$ (100)	LMCT	0.74		0.89		
1^2E	$46e\downarrow \rightarrow 27a_1\downarrow$ (99)	LMCT/(d_π, d_{z^2})	0.63 (0.00002)	0.61[e] (1^2B_1)	0.74 (0.00001)	0.72[e,f](1^2B_1)	

[a] Numbering and composition of the states refer to TDDFT calculations in the gas phase. [b] Oscillator strengths in parentheses. [c] In toluene solution, from this work. [d] In CH₂Cl₂ solution, from this work. [e] The energy value refers to the Jahn–Teller-distorted C_{2v} geometry. [f] Computed at the geometry optimized in the gas phase (C_{2v} symmetry).

to be less than 0.1 eV lower than the corresponding vertical absorption energies.[10,38] In this work, geometry-relaxation effects on the excited states were analyzed only for the lowest ^{2}LMCT state, 1^2B_1, and one of the two ^{2}LMCT states (1^2A_2) lying vertically between the $^2S_1(\pi, \pi^*)$ and $^2T_1(\pi, \pi^*)$ states (the behavior of the 2^2E state was expected to be similar). The relative positions of the 1^2A_2 and 2^2E LMCT states with respect to the $^{2,4}T_1$ set and of the 1^2B_1 state with respect to the ground state are expected to be crucial in interpreting the pathway for deactivation of the $^2S_1(\pi, \pi^*)$ state in CuNc(OBu)$_8$.

The E_{adia} value computed for the 1^2A_2 excited state (see Table 3) suggests that the minimum of the relaxed energy surface of this state (and presumably that of 2^2E also) is well above the minima of the relaxed energy surfaces of the $^2T_1(\pi, \pi^*)$ and $^4T_1(\pi, \pi^*)$ states. Hence, the 1^2A_2 and 2^2E LMCT states are expected to play a role only at the early stage of the deactivation mechanism. As for the lowest LMCT state, 1^2B_1, the minimum of its relaxed energy surface is predicted to lie only 0.25 eV above the minimum of the ground-state surface. The significant decreases (0.17 and 0.13 eV, respectively) in the adiabatic energies of the 1^2A_2 and 1^2B_1 LMCT states with respect to the corresponding vertical absorption energies indicate that the relaxed geometries of these states show significant changes compared to the ground-state geometry. As can be seen in Table S1 in the Supporting Information, which contains optimized geometrical parameters of the 1^2A_2 and 1^2B_1 excited states (and, for the sake of comparison, those of the ground state), the relaxed geometries of these states are characterized by a sizable (∼0.04 Å) lengthening of the Cu−N$_p$ distances and

expansion of the macrocycle core. These geometrical changes are clearly related to occupation of the $27b_2(d_{x^2−y^2})\downarrow$ spin orbital.

The TDDFT results in toluene ($\epsilon = 2.38$) and benzonitrile ($\epsilon = 26.00$) reported in Table 3 show that the vertical absorption energies of the excited states with π, π^* character were scarcely (if at all) affected by solvation. However, the vertical absorption energies of the LMCT states were shifted upward by ∼0.1 eV in toluene and ∼0.2 eV in benzonitrile. As a result, the higher-energy ^{2}LMCT states did not lie below the $^2S_1(\pi, \pi^*)$ state in these solvents. In turn, the lowest LMCT state, 1^2B_1, moved closer to the $^4T_1$ state, particularly in benzonitrile. Interestingly, the oscillator strength of the 2^2E LMCT state in benzonitrile was significantly larger than that in either toluene or the gas phase (see Table 3), which can be explained by the admixture of the more-intense $27b_2\uparrow \rightarrow 47e\uparrow$ transition into the $46e\downarrow \rightarrow 27b_2\downarrow$ transition.

In regard to the solvation model adopted in the calculations of the excited states, it should be stressed here that since the COSMO surface charges are not explicitly considered in the TDDFT procedure other than through their influence on the ground-state density (see Quantum Chemical Calculations in the Experimental Section), changes in vertical excitation energies upon solvation only reflect changes in the energies of the ground-state molecular orbitals. In toluene and, to a greater extent, in benzonitrile, the occupied and virtual ligand orbitals undergo a generalized stabilization, whereas the spin-up and spin-down components of the $27b_2(d_{x^2−y^2})$ MO do not experience significant changes in energy. This explains why the excited states with π, π^* character are affected very little by solvation and the LMCT transitions undergo an upshift.

The higher the polarity of the solvent, the more pronounced the upshift is.

When both solvation and geometry-relaxation effects were taken into account, the minimum of the relaxed energy surface of the 1^2A_2 state was moved back between those of the $^2S_1(\pi, \pi^*)$ and $^2T_1(\pi, \pi^*)$ states (see E_{adia} in Table 3). It is not unreasonable to assume that this holds true also for the 2^2E LMCT state. As for the lowest LMCT state, 1^2B_1, the minimum of its relaxed energy surface was predicted to lie at 0.33 eV in toluene and 0.40 eV in benzonitrile, indicating that the energy gap between this state and the higher-energy $^4T_1$ state decreases when the dielectric constant of the solvent is increased.

CoNc(OBu)$_8$. The vertical absorption energies and oscillator strengths of the excited states of the cobalt complex given in Table 4 clearly indicate that the 4^2E state, which was computed to lie at 1.39 eV (892 nm) in both the gas phase and toluene solution, is responsible for the intense Q(0, 0) band with a maximum at 832 nm and an oscillator strength of 0.540. The calculations also account for the small (~20 nm) blue shift of this band observed in moving from CuNc(OBu)$_8$ to CoNc(OBu)$_8$. The $^2T_1(\pi, \pi^*)$ (2^2E) and $^4T_1(\pi, \pi^*)$ (1^4E) excited states were computed to have gas-phase energies of 0.95 and 0.93 eV, respectively, and nearly identical E_{va} values were obtained in toluene (Table 4).

The $^2T_1(\pi, \pi^*)$ and $^4T_1(\pi, \pi^*)$ excited states, as well as the $^2S_1(\pi, \pi^*)$ state with which they share a common electronic origin, were computed to have slightly higher energies in the cobalt complex than in the copper analog. The vertical absorption energy computed for $^4T_1(\pi, \pi^*)$ suggested that this state be assigned to the weak feature ($f = 0.0006$) appearing at 1332 nm in the near-IR spectrum of CoNc(OBu)$_8$. The observed blue shift of this band in going from the copper to the cobalt complex (1332 vs 1440 nm) further supports this assignment.

TDDFT results indicate that four excited states lie vertically between the $^2S_1(\pi, \pi^*)$ state and the $^{2,4}T_1(\pi, \pi^*)$ set. These are the 2^2A_2, 1^4A_2, 1^2B_1, and 3^2E states. According to the composition of the BP/ALDA solution vectors in Table 4, the nearly degenerate 2^2A_2 and 1^4A_2 states have LMCT character involving transitions from the G-HOMO into the Co–N$_p$ σ antibonding $27b_2\uparrow$ spin orbital. The 1^2B_1 state has pure (d, d) character, while the 3^2E state has mixed LMCT/(d$_\pi$, d$_{z^2}$) character, since it involves a transition out of $45e\downarrow$, which is largely a π orbital of the macrocycle with a 35% contribution from Co $3d_\pi$. The TDDFT results in toluene show that none of these states was significantly affected by solvation. Further inspection of the vertical absorption energies gathered in Table 4 indicates that there are two close-lying excited states, 1^2A_2 and 1^2E, located vertically below the $^{2,4}T_1(\pi, \pi^*)$ set. The former is a pure $19a_2\downarrow \rightarrow 27a_1\downarrow$ LMCT state, while the latter (similar to the higher-energy 3^2E state) has mixed LMCT/(d$_\pi$, d$_{z^2}$) character. Since the results of the ultrafast experiments (Figure 7) clearly demonstrated participation of a (d, d) state in the ground-state repopulation process and the 1^2E state is the most plausible candidate, we decided to ascertain whether the (d, d) character of this state became more pronounced in its
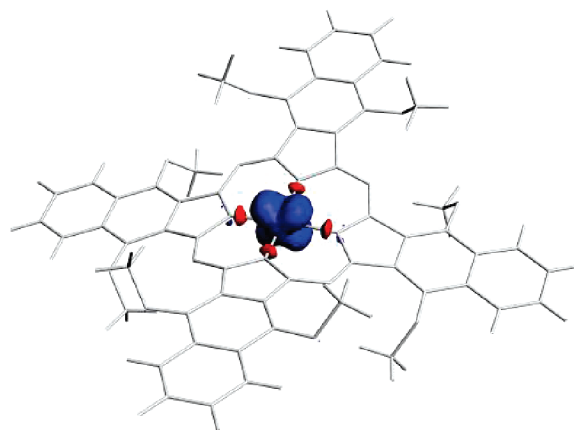

Figure 13. Spin density distribution of CoNc(OMe)$_8$ in the 1^2B_1 excited state.

relaxed geometry. The 1^2E state is doubly degenerate and is expected to undergo Jahn–Teller distortion along the b_1 or b_2 active mode into a D_2 or C_{2v} structure, respectively. Indeed, geometry optimization of 1^2E indicated that the D_{2d} symmetry was no longer stable for this state and was lowered to C_{2v}. The resulting 1^2B_1 electronic state failed to show significant geometrical relaxation, as can be inferred from the geometrical parameters gathered in Table S2 in the Supporting Information. In line with the minor conformational relaxation, the adiabatic energy of the 1^2B_1 state was only 0.01 eV lower than the vertical absorption energy (see Table 4). Analysis of the electron density distribution of CoNc(OMe)$_8$ in its 1^2B_1 excited state indicated that the spin density is mainly localized on the cobalt atom, having Co $3d_{xz}$ as the contributing orbital, with very small districts of opposite spin on the N$_p$ atoms (see Figure 13 for a plot of the spin density distribution). Accordingly, the Mulliken charge on the cobalt atom in the 1^2B_1 state did not change significantly with respect to the ground-state value (+0.63 vs +0.71).

Therefore, if populated, the 1^2E (1^2B_1) excited state is expected to show the derivative-shaped transient absorption difference spectrum characteristic of a (d, d) state. The excited-state pattern as derived from gas-phase TDDFT calculations was not modified when solvent effects were taken into account.

E. Deactivation Mechanism of the Excited States. To elucidate the mechanism of the excited-state deactivation and gain an insight into the effect of the metal on the relaxation processes, the results of the transient absorption experiments on the first-row transition-metal naphthalocyanines considered here were assimilated with those of TDDFT studies. The combination of theoretical and experimental results can provide a comprehensive picture of the photophysical properties of the compounds and an understanding of the fundamental processes that take place after photoexcitation. This knowledge is essential for pursuing the idea of using these compounds in photothermal therapy.

CuNc(OBu)$_8$. The earliest absorption spectral feature detected in CuNc(OBu)$_8$ after photoexcitation with 800 nm light was a broad positive band between 510 and 740 nm with negative bands at wavelengths where the ground-state

species absorbs, i.e., at 480, 755, and 850 nm (Figure 4a,b). By analogy with the Ni(II) variant,[10] this first observed transient (FOT) was assigned to an excited state localized on the π system, most likely the $^2S_1(\pi, \pi^*)$ state (see below). During the first few hundreds of femtoseconds of the experiment, the spectral shape of this transient underwent only minor changes characterized by the small rise of the positive absorption (Figure 4a inset). The lifetime of this rise was estimated to be ~200 fs (Figure 6). Given the similarity of the $S_1(\pi, \pi^*)$ and $T_1(\pi, \pi^*)$ absorption spectra previously observed for metallophthalo- and metallonaphthalocyanines,[10,24,25] we conclude that this ~200 fs process is internal conversion within the doublet manifold ($^2S_1 \rightarrow {}^2T_1$). Support for this assignment comes from the observation of weak fluorescence from the Q state observed during the static emission experiment (Figure 3). The measured fluorescence quantum efficiency of ~3×10^{-4} is consistent with a lifetime of 200 fs for the emitting state. The calculations done here (Table 3) indicate that at least one ^{2}LMCT state (the 1^2A_2) lies adiabatically between the $^2S_1(\pi, \pi^*)$ and $^2T_1(\pi, \pi^*)$ states. This intermediate state is likely to facilitate the $^2S_1 \rightarrow {}^2T_1$ internal conversion.

The decay of the $^2T_1$ state to the ground state showed excellent isosbestic behavior and followed a single-exponential kinetic law characterized by a lifetime of ~1 ns. The isosbestic behavior indicates that the $^2T_1 \rightarrow {}^2S_0$ transition occurs without the intervention of states having significant lifetimes compared with 1 ns. Table 3 shows that a $^4T_1$ state lies very close in energy to the $^2T_1$ state, and below that is an LMCT state (1^2B_1). Either or both of these could be involved in ground-state repopulation, but the transient absorption data do not provide insight on this question. In the static luminescence experiment (Figure 3), the CuNc(OBu)$_8$ complex showed a weak shoulder at ~1172 nm in the red tail of the Q-state fluorescence and a distinct peak at 1460 nm; these features were assigned (see above) to radiative transitions from the $^2T_1$ (tentative) and $^4T_1$ states, respectively. This suggests that the $^4T_1$ state plays a role in the overall deactivation of the $^2T_1$ state. However, the extent of this role is probably quite small, as the emission signals were extremely weak. On balance, the tentative conclusion regarding deactivation of the $^2T_1$ state is that the $^2T_1 \rightarrow {}^4T_1$ and $^2T_1 \rightarrow {}^2$LMCT processes are competing deactivation pathways, with the latter, a spin-allowed process, being strongly favored. In both cases, the intermediate states would have to have short lifetimes (<100 ps) in order to allow the observed isosbestic behavior.

If an LMCT state were involved, its energy would be sensitive to a change of solvent polarity. To investigate this possibility, the pump–probe experiment was repeated in benzonitrile solution. The results showed that the decay of the $^2T_1$ state was enhanced and the isosbestic behavior was retained. Transient kinetic profiles taken at 850 nm and normalized to unit ΔA are shown for toluene and benzonitrile solutions of CuNc(OBu)$_8$ in Figure 14. In benzonitrile, repopulation of the ground state is clearly faster (having a lifetime of ~800 ps). This effect of a solvent with a high dielectric constant on the rate of the ground-state repopulation
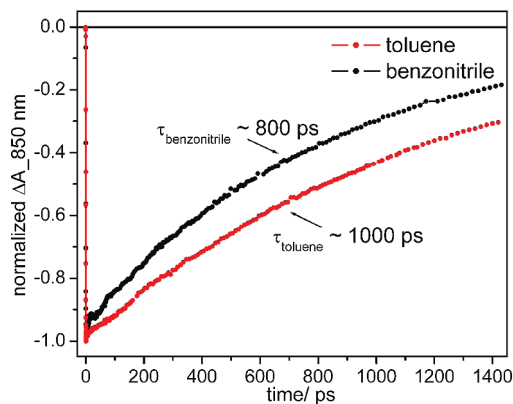

Figure 14. Normalized kinetic profiles of the transient absorption signals at 850 nm for CuNc(OBu)$_8$ in two different solvents obtained after photoexcitation at 800 nm.

process supports the contention that the rate-determining step in the deactivation involves, at least in part, an LMCT state. In the higher-dielectric medium, the LMCT state, which remains spectrophotometrically undetectable, causes the ground-state repopulation process to be more efficient as a result of the energy shift relative to the ground state. Indeed, when the energy of the 1^2B_1 LMCT state was recalculated in toluene and benzonitrile solution (Table 3), sizable destabilization of this state in the more polar solvent (benzonitrile) was observed, with the LMCT state located 0.1 eV closer to the $^2T_1$ state compared to the situation in toluene; this result supports the experimental observation of faster ground-state repopulation in the more polar solvent.

CoNc(OBu)$_8$. The evolution of the transient absorption of CoNc(OBu)$_8$ in toluene solution after photoexcitation at 845 nm (Figure 7) revealed two phases in the process of relaxation to the ground state. The first phase was characterized by a fast decay (having a lifetime of ~1 ps) of the positive absorption signal stretching from 500 to 720 nm accompanied by a complex evolution of the alternating negative and positive absorption bands in the 740–760 and 820–920 nm regions. This complex evolution included blueshifting and narrowing of the derivative-shaped signal accompanied by wavelength-dependent kinetics. The second phase involved a decay of the derivative-shaped band to a zero baseline with isosbestic behavior and a lifetime of 15 ps (Figure 7a inset). The observed feature in the difference spectrum having alternating negative and positive lobes has been well established to arise from the formation of a metal-excited (d, d) state.[37,38,66–69] Thus, it can be concluded that the second kinetic phase represents repopulation of the ground state from a metal (d, d) state. However, the measured lifetime of 15 ps is much shorter than the typical lifetimes of 220–500 ps exhibited by the lowest (d, d) states in common Ni porphyrins[37,70,71] and phthalocyanines[10,38] but comparable to that measured for Co(II) porphyrins (~12

(66) Rodriguez, J.; Holten, D. *J. Chem. Phys.* **1989**, *91*, 3525.
(67) Rodriguez, J.; Kirmaier, C.; Holten, D. *J. Am. Chem. Soc.* **1989**, *111*, 6500.
(68) Rodriguez, J.; Kirmaier, C.; Holten, D. *J. Chem. Phys.* **1991**, *94*, 6020.
(69) Kim, D.; Kirmaier, C.; Holten, D. *Chem. Phys.* **1983**, *75*, 584.
(70) Kim, D.; Holten, D. *Chem. Phys. Lett.* **1983**, *98*, 584.
(71) Kim, D.; Kirmaier, C.; Holten, D. *Chem. Phys.* **1983**, *75*, 305.

ps).[72] The TDDFT results (Table 4) suggest that the experimentally observed (d, d) state is the $1^2E(d_\pi, d_{z^2})$ state, and its short lifetime ($\sim$15 ps) is consistent with this state having quite a low energy (0.72 eV in toluene) and the same multiplicity as the ground state.

In regard to the FOT, the broad positive absorption around 600 nm is reminiscent of the spectra of (π, π^*) excited states of other naphthalocyanine complexes.[10,16,73] Since no detectable Q-state fluorescence was observed during the static luminescence measurements (in contrast to what was observed for the Cu complex), it is very likely that the Q-state lifetime is extremely short and that this state generates the $^2T_1$ state within the instrument response time ($\sim$200 fs). Moreover, the TDDFT computations (Table 4) showed the existence of several excited states between the Q state and the $^2T_1$ state; these are likely to assist the efficient internal conversion of the Q state to the $^2T_1(\pi, \pi^*)$ state. The participation of the $^2T_1$ state in the deactivation pathways could be further supported by the weak emission observed for the cobalt complex at $\sim$1092 nm.

The significant positive absorption band detected to the red of the Q-band bleaching of the FOT is characteristic of a hot (d, d) state, as observed in most nickel porphyrins and phthalocyanines[37,66,68,74–76] but not observed here in the case of the copper variant, which showed no (d, d) state formation. Thus, the first observed transient is probably a composite of the absorptions of the $^2T_1(\pi, \pi^*)$ and metal-centered $1^2E(d_\pi, d_{z^2})$ excited states. The question is whether the π-localized state, the broad positive absorption at 650 nm with a lifetime of 1 ps, decays directly to the ground state or forms the $^2(d_\pi, d_{z^2})$ state.

In the 550–710 nm region, where the ground state of CoNc(OBu)$_8$ absorbs negligibly or not at all, the evolution of the transient absorption signal represents only the decay of the (π, π^*) excited state(s). However, in the 740–840 nm region, where the ground state has a significant extinction coefficient, the kinetic traces represent a superposition of the temporal progressions of both the positive absorption and the ground-state recovery. Thus, the evolution of the transient absorption signal in this region is a sum of these two processes weighted by contributions from the extinction coefficients of the ground- and excited-state species. The reduction in the intensity of the negative absorption bands observed in Figure 7 during the first 3−4 ps is too large to be explained solely by an increase in the $^2(d_\pi, d_{z^2})$ extinction coefficient at these wavelengths during the vibrational cooling process. The large decrease in bleaching intensity is most likely to be the result of repopulation of the ground state. Thus, the $^2T_1$ state, which is populated from the initially produced Q state in competition with the formation of the
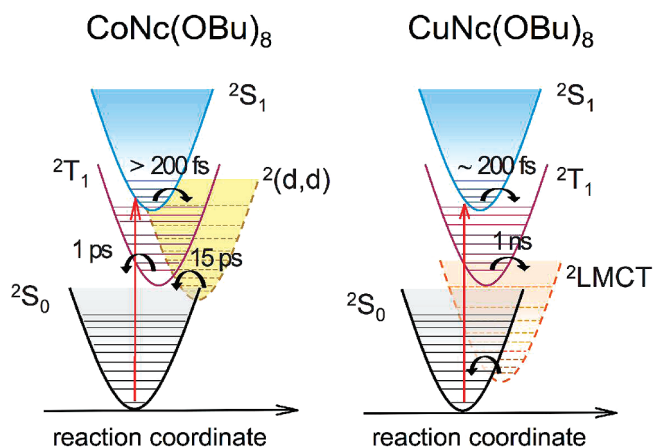
(72) Loppnow, G. R.; Melamed, D.; Leheny, A. R.; Hamilton, A. D.; Spiro, T. G. *J. Phys. Chem.* **1993**, *97*, 8969.
(73) Firey, P. A.; Rodgers, M. A. J. *Photochem. Photobiol.* **1987**, *45*, 535.
(74) Eom, H. S.; Jeoung, S. C.; Kim, D.; Ha, J. H.; Kim, Y. R. *J. Phys. Chem. A* **1997**, *101*, 3661.
(75) Drain, C. M.; Kirmaier, C.; Medforth, C. J.; Nurco, D. J.; Smith, K. M.; Holten, D. *J. Phys. Chem.* **1996**, *100*, 11984.
(76) Drain, C. M.; Gentemann, S.; Roberts, J. A.; Nelson, N. Y.; Medforth, C. J.; Jia, S.; Simpson, M. C.; Smith, K. M.; Fajer, J.; Shelnutt, J. A.; Holten, D. *J. Am. Chem. Soc.* **1998**, *120*, 3781.

Figure 15. Schematic diagrams showing the proposed excited-state relaxation pathways for (left) CoNc(OBu)$_8$ and (right) CuNc(OBu)$_8$ in toluene.

hot $^2(d_\pi, d_{z^2})$ state, decays to the ground-state surface while the metal-centered state undergoes vibrational relaxation. The ^{2}LMCT state, theoretically predicted to lie below the set of triplets, enhances internal conversion from the $^2T_1$ state to the ground state.

In summary, after the Q state is generated by photoexcitation, it deactivates within the instrument response time through two channels. One channel leads to the formation of the $^2T_1$ state localized on the π system, while the other leads to the vibrationally hot $^2(d_\pi, d_{z^2})$ state. Thus, the FOT is a superposition of the absorption spectra of the $^2T_1(\pi, \pi^*)$ and hot $^2(d_\pi, d_{z^2})$ states. The $^2T_1(\pi, \pi^*)$ state decays back to the ground state with a lifetime of 1 ps while the $^2(d, d)$ state experiences a vibrational cooling process. After the cooling process is complete, the $^2(d, d)$ state repopulates the ground state with a lifetime of 15 ps.

To summarize the above conclusions, diagrams illustrating the pathways for deactivation of the excited Q states of the Co(II) and Cu(II) octabutoxynaphthalocyanine complexes in toluene are shown in Figure 15.

Concluding Remarks

Transient absorption experiments have shown that changing the central metal M from Co through Ni to Cu results in striking differences in the photophysical behavior of the MNc(OBu)$_8$ complexes. Variations in the lifetimes for repopulation of the ground state from tens of picoseconds to nanoseconds were observed across the MNc(OBu)$_8$ (M = Co, Ni, Cu) series. These differences can be rationalized in terms of significant changes induced by the central metal in the nature and energies of the excited states involved in the decay route of the primarily photogenerated Q state. It is instructive in this regard to compare the photophysical behavior of NiNc(OBu)$_8$ and CuNc(OBu)$_8$. For both of these complexes, transient absorption experiments and TDDFT calculations suggest that repopulation of the ground state proceeds from triplet states localized on the π system with participation of the LMCT(π, $d_{x^2-y^2}$) state. However, in the Cu complex, this process takes twice as long as in the Ni complex. The vertical absorption energies calculated for the

$T_1(\pi, \pi^*)$ state in the nickel complex and the $^{2,4}T_1(\pi, \pi^*)$ pair of states in the copper complex do not differ significantly; however, the LMCT state of the Cu complex is much lower in energy than that of the Ni complex (0.38 vs 0.84 eV), with the result that in the Cu complex, the rate-determining process is the intrinsic decay of the $^2T_1(\pi, \pi^*)$ state to the lower-lying LMCT state. In the Ni variant, the LMCT state is in equilibrium with the nearly degenerate $T_1(\pi, \pi^*)$ state, resulting in the observed facile ($\sim$500 ps) repopulation of the ground state.

Nevertheless, a thorough understanding of the variations in the ground-state repopulation rates as a function of the coordinated metal remains elusive. The underlying difficulty in this quest is that theory provides thermodynamic data (i.e., the energies of states that possibly contribute to the decay routes), which is not necessarily relevant to an examination of rate processes. What is really required is information about the topography of the excited-state surfaces, such as the locations of intersections and the heights of energy barriers. However, for large molecules such as those considered here, such information is beyond the realm of the extant methodologies. As a matter of fact, location of intersections has been done for small molecules using TDDFT methods, although the applicability of TDDFT using modern functionals when conical intersections are involved is currently not completely clear.[77]

Another question concerning the photophysics of the copper and cobalt complexes that remains unanswered is whether, and to what extent, the $^4T_1$ state is involved in the deactivation mechanism. Knowledge about the efficiency of the $^2T_1 \rightarrow {}^4T_1$ intersystem crossing process would represent a step forward in this direction. This could be achieved through explicit calculations of the spin–orbit coupling between these states, for which the relativistic spin–orbit zero-order regular approximation (ZORA) formalism[78–80]

implemented in ADF would be adequate. Unfortunately, ZORA spin–orbit-coupled TDDFT calculations are currently restricted to closed-shell systems.

In spite of the differences observed in their photophysical behavior, CoNc(OBu)$_8$ and CuNc(OBu)$_8$ (as well as the previously investigated Ni variant) fulfill the fundamental requirements for consideration as photothermal sensitizers for in vivo use: they have intense, far-red optical absorptions, and their excitation energies are rapidly dissipated through radiationless channels. The results described in this work present necessary background and basic knowledge in support of the prospective use of these compounds in photothermal therapeutic applications.

Supporting Information Available: Optimized geometrical parameters for the 1^2A_2 and 1^2B_1 excited states of CuNc(OMe)$_8$ (Table S1) and the 1^2B_1 excited state of CoNc(OMe)$_8$ (Table S2). This material is available free of charge via the Internet at http://pubs.acs.org.

IC7023204

(77) Levine, B. G.; Ko, C.; Quenneville, J.; Martinez, T. J. *Mol. Phys.* **2006**, *104*, 1039.

(78) van Lenthe, E.; Baerends, E. J.; Snijders, J. G. *J. Chem. Phys.* **1993**, *99*, 4597.

(79) van Lenthe, E.; Baerends, E. J.; Snijders, J. G. *J. Chem. Phys.* **1994**, *101*, 9783.

(80) van Lenthe, E.; Ehlers, A. W.; Baerends, E. J. *J. Chem. Phys.* **1999**, *110*, 8543.